Inverse Heat Transfer Solution of the Heat Flux Due to Induction Heating

Jie Luo
Graduate Research Assistant

Albert J. Shih[1]
Associate Professor
e-mail: shiha@umich.edu

Department of Mechanical Engineering,
University of Michigan,
Ann Arbor, MI 48109-2125

The explicit finite difference formulation of an inverse heat transfer model to calculate the heat flux generated by induction is developed. The experimentally measured temperature data are used as the input for the inverse heat transfer model. This model is particularly suitable for a workpiece with low cross section Biot number. Induction heating experiments are carried out using a carbon steel rod. The finite difference method and thermocouple temperature measurements are applied to estimate the induction heat flux and workpiece temperature. Compared to measured temperatures, the accuracy and limitation of proposed method is demonstrated. The effect of nonuniform temperature distribution, particularly in the heating region during the induction heating, is studied. Analysis results validate the assumption to use the uniform temperature in a cross section for the inverse heat transfer solution of induction heat flux. Sensitivity to the grid spacing, thermocouple location, and thermophysical properties are also studied.
[DOI: 10.1115/1.1949617]

1 Introduction

Induction heating is a process involving the interaction of both electromagnetic and thermal transport. An eddy current is generated in the workpiece by the varying electromagnetic field produced by the alternating electrical current passing through the water-cooled induction coils. The majority of heat generated by the eddy current due to the Joule heating effect is concentrated in a surface layer of the workpiece. The thickness of this layer, called penetration depth, depends on the electromagnetic field frequency and material properties and is usually very small. The heat generated by induction can be modeled as the workpiece surface heat flux [1]. For electrically conductive work-materials, the induction heating can quickly and accurately produce a desired temperature profile at selected locations. It is a convenient, noncontact heating method widely used in industry for applications such as the heat treatment (hardening, tempering, and annealing), melting, welding, and joining [2–5].

The design of induction heating systems needs to determine the heat generation and the resulting temperature profile in the workpiece. The rate of heat generated in the workpiece is determined by the magnetic and thermal properties of the work-material, electrical current through the induction coil, geometry, position and shape of the coil around the workpiece, as well as many other factors. Numerical modeling, which includes the magnetic and thermal analysis, has been applied to design the induction heating system [2]. The finite element [6–13] and finite difference [14–17] methods have been applied to analyze the electromagnetic field generated by the coil for induction heating. The magnetic vector potential is calculated from the Maxwell's equations and applied to solve the induction heat generation rate or heat flux in the workpiece [6–8,16].

The magnetic permeability of the work-material is a key, but difficult to be accurately determined, parameter to solve the Maxwell's equations. The magnitude of magnetic permeability varies due to the change of magnetic field, temperature, as well as the alloy composition, impurities, and heat treatment of the work-material [13]. Wang et al. [6–8] and Maten and Melissen [9] include the transition of magnetic permeability at Curie temperature and assume that the magnetic permeability is independent of magnetic field. More comprehensive magnetic permeability models, which consider the influence of temperature [10], magnetic intensity [11,12,15,17], or the combination of both temperature and magnetic intensity [14,16], have been developed to study the induction heating process. For newly developed materials, the comprehensive model of the magnetic permeability is also lacking. This has limited the capability to use numerical methods to determine the induction heat flux and the subsequent workpiece thermal modeling.

The goal of this research is to develop a method to experimentally determine the heat flux generated by induction without the information of the magnetic permeability and modeling of the magnetic field. The inverse heat transfer method [18] is applied. The temperature data measured by a thermocouple located near the induction heated region is used to estimate the heat flux generated on the workpiece surface. This method is suitable for a workpiece, such as the shaft and rod, with small variation of temperature across the cross section, when a single value can represent the temperature in the cross section. Based on this approach, an explicit finite difference model is developed to solve the inverse heat transfer problem and to find the induction heat flux based on experimental measurement.

The mathematical modeling is summarized in the following section. Setup of the induction heating experiments and configuration for temperature measurement are then presented. Experimental results and validation of heat flux estimated using the inverse heat transfer model are discussed in Sec. 4. Sensitivity to the grid spacing, thermocouple location, and thermophyciscal properties is investigated in Sec. 5. Finally, an example using the estimated heat flux as the input for finite element thermal analysis of induction heating is analyzed and results are compared with the finite difference prediction.

2 Mathematical Modeling

The finite difference method is developed to solve the inverse heat transfer problem to estimate the surface heat flux generated by induction. The mathematical model developed in this study is targeted for the induction heating of a long and slender shape workpiece, as shown in Fig. 1, with low cross-section Biot number (Bi). The effect of the Biot number, explicit finite difference

[1]Author to whom correspondence should be addressed.

Contributed by the Manufacturing Engineering Division for publication in the ASME JOURNAL OF MANUFACTURING SCIENCE AND ENGINEERING. Manuscript received July 24, 2003; final revision received July 7, 2004. Associate Editor: S. R. Schmid.

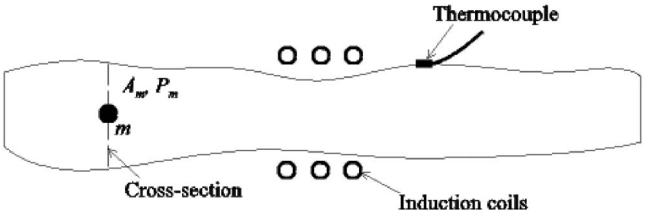

Fig. 1 Configuration of the induction heating a long workpiece and the cross section represented by a node m with area A_m and perimeter P_m

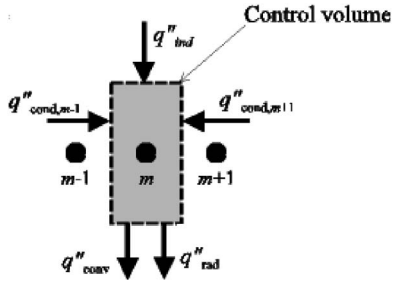

Fig. 3 Control volume at node m and the sources of heat flux

modeling, and inverse heat transfer solution of heat flux generated in induction heating are discussed in the following three sections.

2.1 Effect of the Biot Number. The Biot number is defined as [18]:

$$\mathrm{Bi} = \frac{hL_c}{k} \tag{1}$$

where h is the convention coefficient, k is the thermal conductivity, and L_c is characteristic dimension of the cross section, which is the span in the cross-section area to represent the worst possible condition of temperature variation. For Bi less than 0.1 [19], the temperature of the cross section can be represented by a single value at the node in finite difference analysis.

An example is used to demonstrate the size of a carbon steel cross section that meets the Bi=0.1 criterion. Using the room temperature$k$=52 W/m·K for the carbon steel workpiece, under the free (natural) convection with h=10 W/m^2·K, L_c is 520 mm. This indicates that, for a cross section with characteristic dimension less than 520 mm, regardless of the shape of the cross section, the temperature distribution in the workpiece can be represented by the nodal temperature of a series of connected nodes. Under forced convection with h=200 W/m^2·K, L_c is 26 mm. The high convection coefficient creates larger temperature gradient between the surface and inside of the workpiece and limits the L_c of the cross-section area suitable to be represented by a single temperature.

This example illustrates that, for the metallic material with reasonably high thermal conductivity, a wide range of workpiece cross-section size is applicable using the proposed method. The temperature gradient in the cross section of the workpiece with low Bi number will be further analyzed by using the finite element method later in Sec. 6.

2.2 Explicit Finite Difference Modeling of the Workpiece With Low Cross Section Biot Number. The induction heating coils generate a heating region in the workpiece. The area without heating is referred as the cooling region. Assuming the workpiece is symmetry in the middle of the heating region, an adiabatic boundary condition exists in the middle of the heating region. The origin of the x axis locates on this adiabatic boundary surface. As shown in Fig. 2, half of the workpiece is represented by nodes in both heating and cooling regions. The average temperature of the cross section in the adiabatic boundary surface is denoted as node 1. There are m_1 nodes in the heating region and m_2 nodes in the cooling region. The spacing between two adjacent nodes in the heating and cooling region is Δx_h and Δx_c, respectively. The length of the workpiece is $2L$ and the width of the heating region is $2L_h$. Therefore, $\Delta x_h = L_h/(m_1-1)$ and $\Delta x_c = (L-L_h)/m_2$. The perimeter and area of the cross section at node m is denoted P_m and A_m, respectively. The control volume at node m, as shown in Fig. 3, is V_m. Induction heating starts from time t=0 and ends when $t=t_h$. The heat flux generated in the heating region during heating stage ($0 \leqslant t \leqslant t_h$) is assumed uniform. When $t > t_h$, heating stops and the whole workpiece is cooled under the convection and radiation.

Based on the energy balance method, explicit finite difference equations are derived for the heating and cooling stages.

2.2.1 Heating Stage, $0 \leqslant t \leqslant t_h$. As shown in Fig. 3, the energy exchange in the control volume at node m is influenced by the conduction between the node m and adjacent nodes $m-1$ and $m+1$ and the convection, radiation, and induction heat generation on the peripheral surface $P_m \Delta x, \Delta x$ is the width of the control volume. The conduction rate from node $m-1$ to m and from node $m+1$ to m is represented by heat flux $q''_{\mathrm{cond},m-1}$ and $q''_{\mathrm{cond},m+1}$, respectively. The heat flux due to convection and radiation on the

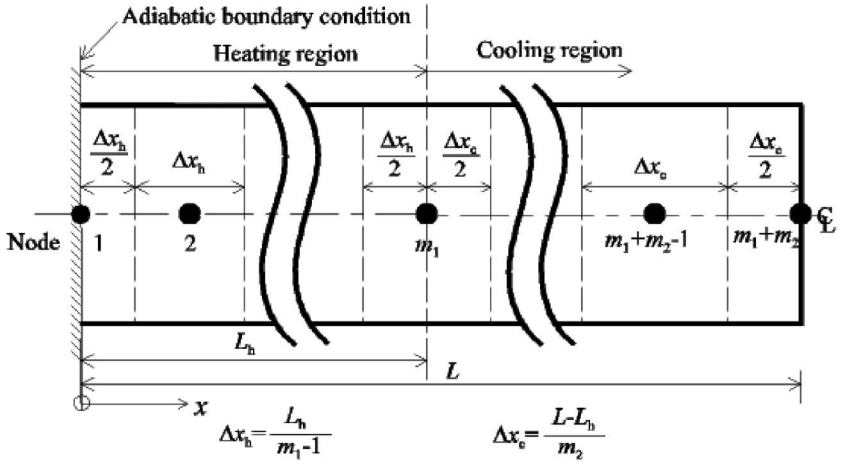

Fig. 2 Finite difference model and nodal points in a half rod

peripheral surface of the control volume at node m is q''_{conv} and q''_{rad}, respectively. A uniform heat flux q''_{ind} is applied on the surface of the peripheral heating region. Based on the finite difference method, the energy balance of the control volume at node m can be derived as

$$(q''_{cond,m-1} + q''_{cond,m+1}) \cdot A_m + (q''_{ind} - q''_{conv} - q''_{rad}) \cdot P_m \cdot \Delta x = \rho c \cdot A_m \Delta x \cdot \frac{T_m^{p+1} - T_m^p}{\Delta t} \quad (2)$$

where ρ is the density, c is the specific heat, Δt is the time increment, and T_m^p is the nodal temperature at node m and time step p.

All the nodes fall into the following three categories: nodes in the heating region, nodes in the cooling region, and boundary nodes.

(i) Nodes in the heating region $(2 \leqslant m \leqslant m_1 - 1)$

The energy balance in the control volume at node m in the heating region during the heating stage can be expressed as:

$$k \cdot A_m \cdot \frac{T_{m+1}^p + T_{m-1}^p - 2T_m^p}{\Delta x_h} + (q''_{ind} - q''_{conv} - q''_{rad}) \cdot P_m \cdot \Delta x_h = \rho c \cdot A_m \Delta x_h \cdot \frac{T_m^{p+1} - T_m^p}{\Delta t} \quad (3)$$

(ii) Nodes in the cooling region $(m_1 + 1 \leqslant m \leqslant m_1 + m_2 - 1)$

For nodes in the cooling region, Eq. (3) with $q''_{ind} = 0$ is the energy balance equation.

(iii) Boundary nodes $(1, m_1, m_1 + m_2)$

Three boundary nodes exist on the adiabatic boundary surface (node 1), at the interface between the heating and cooling regions (node m_1), and at the end of cooling region (node $m_1 + m_2$). To determine the thermal conditions more accurately, the half-width control volumes are assigned to the corresponding boundary nodes.

The energy balance of the control volume at node 1 is

$$k \cdot A_1 \cdot \frac{T_2^p - T_1^p}{\Delta x_h} + (q''_{ind} - q''_{conv} - q''_{rad}) \cdot P_1 \frac{\Delta x_h}{2} = \rho c \cdot A_1 \frac{\Delta x_h}{2} \cdot \frac{T_1^{p+1} - T_1^p}{\Delta t} \quad (4)$$

The energy balance of the control volume at boundary node m_1 is

$$k \cdot A_{m_1} \cdot \left(\frac{T_{m_1+1}^p - T_{m_1}^p}{\Delta x_c} + \frac{T_{m_1-1}^p - T_{m_1}^p}{\Delta x_h} \right) + q''_{ind} \cdot P_{m_1} \frac{\Delta x_h}{2} - (q''_{conv} + q''_{rad}) \cdot P_{m_1} \left(\frac{\Delta x_h}{2} + \frac{\Delta x_c}{2} \right) = \rho c \cdot A_{m_1} \frac{(\Delta x_h + \Delta x_c)}{2} \cdot \frac{T_{m_1}^{p+1} - T_{m_1}^p}{\Delta t} \quad (5)$$

The energy balance of the control volume at boundary node $m_1 + m_2$ is

$$k \cdot A_{m_1+m_2} \cdot \frac{T_{m_1+m_2-1}^p - T_{m_1+m_2}^p}{\Delta x_c} - (q''_{conv} + q''_{rad}) \cdot \left(P_{m_1+m_2} \frac{\Delta x_c}{2} + A_{m_1+m_2} \right) = \rho c \cdot A_{m_1+m_2} \frac{\Delta x_c}{2} \cdot \frac{T_{m_1+m_2}^{p+1} - T_{m_1+m_2}^p}{\Delta t} \quad (6)$$

2.2.2 Cooling Stage, $t > t_h$. No heat flux is generated by induction during the cooling stage. Equations (3)–(6) with $q''_{ind} = 0$ can be used as the finite difference representation of energy balance at all nodes.

2.2.3 Convection and Radiation Heat Flux. A good approximation of the heat flux of a vertical wall due to free convection in air can be expressed using the following equation [4]:

$$q''_{conv} = B(T_m^p - T_\infty)^{1.25} (\mathrm{W/m^2}) \quad (7)$$

where $B = 1.8\ \mathrm{W/m^2 \cdot K^{1.25}}$ for vertical walls, $1.3\ \mathrm{W/m^2 \cdot K^{1.25}}$ for downward inclining horizontal walls, and $1.5\ \mathrm{W/m^2 \cdot K^{1.25}}$ for upward inclining horizontal walls, and T_∞ is the ambient temperature.

The radiation heat flux can be expressed as

$$q''_{rad} = \sigma_s \varepsilon ((T_m^p + 273)^4 - (T_\infty + 273)^4) (\mathrm{W/m^2}) \quad (8)$$

where ε is the emissivity of the work-material and σ_s is the Stefan-Boltzmann constant ($\sigma_s = 5.67 \times 10^{-8}\ \mathrm{W/m^2\ K^4}$).

2.3 Inverse Heat Transfer Solution. The only unknown in the finite difference model presented in Sec. 2.2 to solve the spatial and temporal temperature distribution is the heat flux q''_{ind} in the heating region. The inverse heat transfer method is applied to solve q''_{ind} by using the experimentally measured temperatures at given locations on the workpiece. The measured temperature at the location x_j of thermocouple j and time t_i is denoted as $T^{t_i}_{x_j|exp}$.

Based on finite difference equations in Sec. 2.2, the nodal temperature T_m^{p+1} at node m and time step $p+1$ can be expressed as a function of temperatures T_{m-1}^p, T_m^p, and T_{m+1}^p at prior time step p. The actual value of q''_{ind} is an unknown. Using an estimated value of q''_{ind} and the initial temperature of the workpiece T_m^0 at time step $p=0$, the temperature $T^{t_i}_{x_j|est}$ at location x_j and time t_i can be calculated. The discrepancy between the experimentally measured $T^{t_i}_{x_j|exp}$ and finite difference model estimated $T^{t_i}_{x_j|est}$ depends on the q''_{ind}. An objective function as the summation of the squares of the temperature discrepancy is defined as

$$\mathrm{Obj}(q''_{ind}) = \sum_{i=1}^{n_1} \sum_{j=1}^{n_2} (T^{t_i}_{x_j|exp} - T^{t_i}_{x_j|est})^2 \quad (9)$$

where n_1 is the number of time instants applied in the estimation algorithm, and n_2 is the number of thermocouples applied in the estimation algorithm.

By minimizing $\mathrm{Obj}(q''_{ind})$, the value of q''_{ind} can be obtained. The golden section search method [20] is applied to find q''_{ind} that minimizes $\mathrm{Obj}(q''_{ind})$. A search range for q''_{ind} needs to be determined using the golden section search method. The lower bound of q''_{ind} is 0, which represents that no heat flux is generated during the induction heating. The upper bound is determined by dividing the peak power output of the induction heating power supply and the peripheral surface area of the heating region. The correct value of q''_{ind} that minimizes $\mathrm{Obj}(q''_{ind})$ lies between the upper and lower bounds and can be solved using the golden section search method.

3 Experiment

As shown in Fig. 4, the induction heating experiment was conducted on a vertically suspended AISI 1020 low carbon steel rod, 1140 mm in length ($2L$) and 6.35 mm in radius (r). The water-cooled induction coil, 4 mm in outside diameter, is located in the middle of the rod and creates a 11.3 mm wide ($2L_h$) heating region. An Ameritherm NOVA 1.0 induction heating unit is used to generate the alternating current in the coil, which produces the eddy current and the surface heating of the workpiece. The induction heating system automatically scans the operating frequency range from 50 to 450 kHz and selects the optimum operating

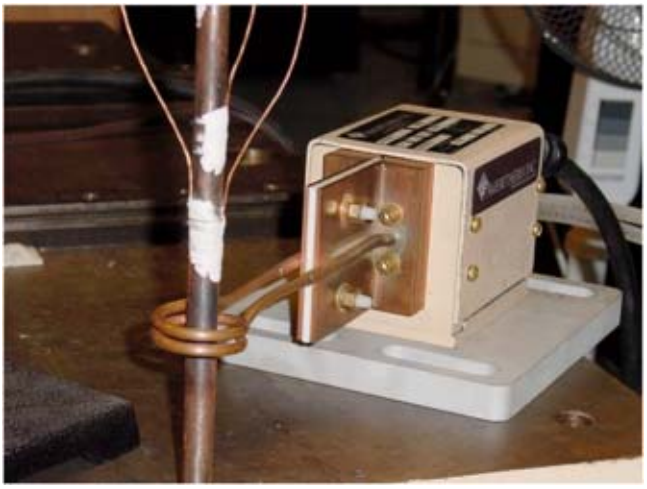

Fig. 4 Setup of rod workpiece, water-cooled induction heating coil, and thermocouples

frequency based on the coil and load combination. For the rod and coil combination shown in Fig. 4, the operating frequency was 270 kHz and the power output was set at 0.8 kW.

Four type *K* thermocouples (Omega CO1-K) with butt bonded junction, tip size of 2.5 mm by 3.0 mm, and 10 to 20 ms response time are attached to the steel rod. As illustrated in the configuration of the induction heating experimental setup in Fig. 5, the location of thermocouple 1 through 4 is marked as x_1 to x_4, respectively. In this study, $x_1=28.6$ mm, $x_2=35.8$ mm, $x_3=68.6$ mm, and $x_4=129.0$ mm. Voltage signals from thermocouples are acquired using a 4-channel PC-based data acquisition system with the 250 Hz sampling rate. During the heating stage, the electromagnetic interference generates noise in the thermocouple voltage output and prohibits the temperature measurement. The measured temperature data is averaged and recorded every 0.5 s.

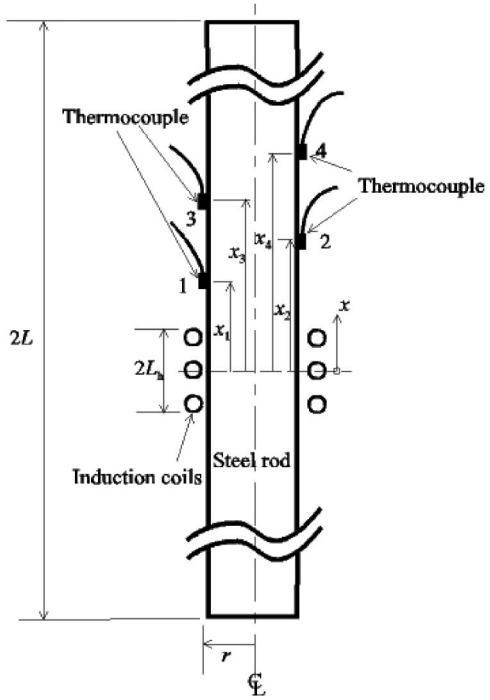

Fig. 5 Configuration of the induction heating experiment of the rod workpiece and thermocouple locations

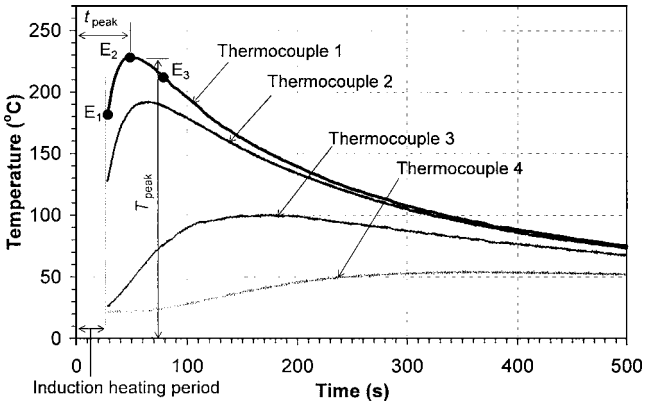

Fig. 6 Experimentally measured temperatures at four thermocouples for $t_h=25$ s and the selection of data points for inverse heating transfer solution of induction heat flux

Three experiments were carried out with the duration of heating t_h set at 15, 20, and 25 s. Each experiment was repeated three times to verify its repeatability.

4 Results

The experimental temperature measurements, calculated induction heat flux and finite difference modeling results, comparison of the experimental and modeling results, and measurement error analysis are discussed in the following sections.

4.1 Experimental Temperature Measurements. Figure 6 shows an example of the measured temperature during the cooling stage at four thermocouples with $t_h=25$ s. For a specific thermocouple, the temperature peaked at time t_{peak}. The magnitude of the peak temperature is denoted as T_{peak}. Since the heat generated by induction transfers like a thermal wave from the heating region toward both ends of the rod, the thermocouple closer to the heating region has higher T_{peak} and lower t_{peak}. The thermal energy is transferred via conduction through the rod. In the meantime, the thermal energy is also dissipated from the peripheral surface by convection and radiation and stored in the rod due to the increase in workpiece temperature and heat capacity, ρc. The loss and storage energy result the reduction in peak temperature T_{peak} for thermocouples away from heating region.

The t_{peak} and T_{peak} at thermocouple 1 for the three repeated tests conducted at $t_h=15$, 20, and 25 s are listed in Table 1. Longer duration of heating t_h delivers more energy to the rod and generates higher temperature T_{peak}. Longer t_h also delays the time t_{peak} for the thermocouple to reach the peak temperature. Three repeated tests show good agreement in T_{peak} with less than 2% discrepancy. However, the maximum discrepancy of t_{peak} is about 11%. This is due to the relatively flat temperature response near the peak. As shown later in Sec. 4.2, such discrepancy does not significantly change the calculated heat flux.

4.2 Calculated Heat Flux and Finite Difference Modeling Results. The finite difference model and inverse heat transfer method presented in Sec. 2 are applied to solve q''_{ind}. The grid with number of nodes in the heating region $m_1=3$ and number of nodes in the cooling region $m_2=201$ is applied in the modeling. The experimentally measured temperature, thermocouple location, and material properties are the required input. For the AISI 1020 steel, $\rho=7870$ kg/m^3, and temperature-dependent properties is obtained by linear interpolation or extrapolation with $c=486$ J/kg$^2\cdot$K and $k=51.9$ W/m$\cdot$K at 20 °C and $c=519$ J/kg$^2\cdot$K and $k=48.9$ W/m$\cdot$K at 200 °C [21]. Equation (7) is used to estimate

Table 1 Measured peak temperature T_{peak} and corresponding time t_{peak} of thermocouple 1

t_h (s)		T_{peak} (°C)	t_{peak} (s)
15	Test I	145.3	41.5
	Test II	144.7	41.5
	Test III	141.7	46.0
	Discrepancy (%)	2.54%	10.80%
20	Test I	187.7	42.0
	Test II	190.0	45.5
	Test III	187.3	46.0
	Discrepancy (%)	1.44%	9.52%
25	Test I	228.0	48.5
	Test II	229.5	53.0
	Test III	232.4	47.5
	Discrepancy (%)	1.93%	11.60%

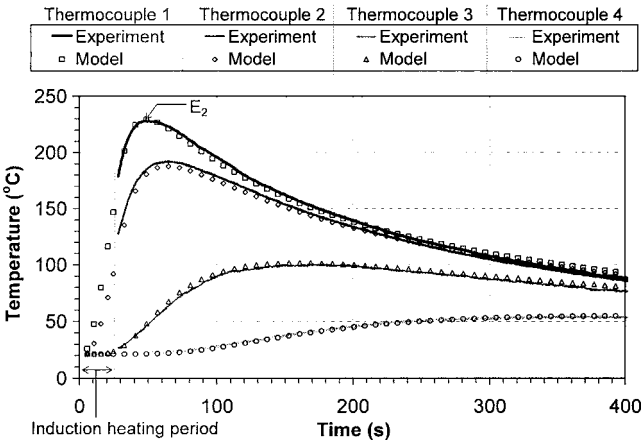

Fig. 7 Comparison of the measured and calculated temperature for t_h=25 s

the convection heat flux with $B=1.8\ \mathrm{W/m^2\cdot K^{1.25}}$. The convection coefficient varies from 0 to 6.8 $\mathrm{W/m^2\cdot K}$ with $T_m^p - T_\infty$ varying from 0 to 200 °C, which corresponds to Bi from 0 to 0.00167. The low Bi confirms that the assumption of uniform temperature in the cross section is suitable for this study. The ambient temperature T_∞ and initial temperature of the rod at $t=0$ are both 21.4 °C. The emissivity for thermal radiation heat flux in Eq. (8) is 0.7 [2].

Many options for selecting experimental data points of measured temperature for minimizing the objective function in Eq. (9) are possible. It can be one point, typically the peak temperature, such as E_2 (48.5 s, 228.0 °C) in Fig. 6. Or, it can be the combination of several points, such as the E_1 (28.5 s, 181.6 °C), E_2, and E_3 (78.5 s, 212.0 °C). When only one data point is used, if the peak temperature is not selected, the modeling usually cannot accurately predict q''_{ind}.

An example is used to illustrate the effect of data points selection. If one data point E_2 in Fig. 6 is used, the calculated q''_{ind} is 1.103 $\mathrm{MW/m^2}$. If E_1,E_2, and E_3 are used, q''_{ind}=1.122 $\mathrm{MW/m^2}$. This demonstrates that one peak temperature data point can provide accurate estimation of q''_{ind}.

Using the T_{peak} and corresponding t_{peak} of the four thermocouples in three repeated tests (tests I, II, and III) of three experiments with t_h=15, 20, and 25 s, results of the 36 (=3×3×4) estimated q''_{ind} are summarized in Table 2. For three repeated tests, the calculated q''_{ind} is very repeatable, less than 3.0% discrepancy, at thermocouples 1, 2, and 3. The slight difference may be caused by inconsistent induction power output at the beginning of the operation, which was observed during the experiments. Relatively high discrepancy, from 2.4% to 10.2%, can be seen in repeated tests conducted using the temperature data of thermocouple 4. The relatively low temperature, flat peaks of temperature profile, and the long distance from the heating region all contribute to the discrepancy in repeated test results. Also seen in the last three rows of Table 2, for experiments at the same t_h, the average q''_{ind} estimated by the peak temperature at four thermocouples has some, but not significant, discrepancy. In summary, Table 2 demonstrates the feasibility of the proposed method to use a single measured temperature data point to estimate the q''_{ind} and the consistency of the induction heating tests.

4.3 Comparison of Experimental and Modeling Results. Based on the calculated induction heat flux q''_{ind}, the temporal and spatial distribution of temperature on the rod can be analyzed using the finite difference method. The T_{peak} and t_{peak} at thermocouple 1 was used to calculate heat flux q''_{ind}. Using this q''_{ind}, the finite difference modeling was used to calculate the temperature. Results of the finite difference modeling (open symbols) and experimental measurement (lines) at four thermocouple locations are illustrated and compared in Fig. 7. A good match can be seen on

Table 2 Calculated induction heat flux q''_{ind}($\mathrm{MW/m^2}$)

	t_h (s)	Test I	Test II	Test III	Average	Discrepancy (%)
Thermocouple 1	25	1.120	1.107	1.132	1.120	2.29%
	20	1.098	1.112	1.099	1.103	1.32%
	15	1.058	1.076	1.081	1.071	2.14%
Thermocouple 2	25	1.155	1.146	1.171	1.157	2.14%
	20	1.139	1.144	1.135	1.139	0.84%
	15	1.094	1.101	1.117	1.104	2.07%
Thermocouple 3	25	1.089	1.102	1.123	1.105	3.12%
	20	1.047	1.072	1.070	1.063	2.34%
	15	1.034	1.063	1.033	1.043	2.97%
Thermocouple 4	25	1.120	1.148	1.134	1.134	2.49%
	20	1.071	1.085	1.060	1.072	2.40%
	15	1.028	1.120	1.016	1.055	10.23%
Discrepancy of average induction heat flux	25				4.71%	
	20				7.15%	
	15				5.85%	

point E_2, the location of T_{peak} and t_{peak} of thermocouple 1.

The root mean square (rms) error, e_{rms}, is defined as follows [18]:

$$e_{rms} = \sqrt{\frac{1}{N}\sum_{i=1}^{N} (T^{t_i}_{x_j|exp} - T^{t_i}_{x_j|est})^2} \quad (10)$$

where N is the number of measurements.

The e_{rms} is calculated at each thermocouple to quantity the discrepancy between the experimental and modeling temperature results.

As shown in Fig. 7, temperatures at four thermocouples were measured when $28 < t < 400$ s. At each thermocouple, a total of 744 measurements were conducted. The e_{rms} of thermocouple 1, 2, 3, and 4 is equal to 2.6, 3.7, 2.9, and 1.0 °C, which is 1.13%, 2.02%, 2.85%, and 1.82% of its corresponding T_{peak}, respectively. The e_{rms} is due to the measurement errors and approximation of temperature-dependent thermophysical properties. The effect of measurement errors is discussed in the next section.

It is noted that, since the q''_{ind} is calculated using the data of T_{peak} and t_{peak} of thermocouple 1, the error at thermocouple 1 is the lowest. Also, the finite difference modeling is able to predict the workpiece temperature during the heating stage ($0 < t < 25$ s), as the information not available in thermocouple-based experimental measurement. This is shown by the open symbols in Fig. 7.

4.4 Measurement Error Analysis. Four measurement errors and uncertainties have been identified as the key parameters that affect the estimated heat flux q''_{ind}. These four parameters are: (1) the error of measured peak temperature T_{peak}; (2) the error of ambient temperature T_∞; (3) the uncertainty of thermocouple location x_j; and (4) the uncertainty of the instant for peak temperature t_{peak}. Based on experimental data, the 95% confidence interval of the temperature reading is ±0.8 °C. This is used as the error of T_{peak} and T_∞. The uncertainty of t_{peak} is assumed as ±0.25 s (the interval of temperature data reading) and the uncertainty of x_j is assumed as ±1.5 mm (the tip size of the thermocouple).

Higher T_{peak}, t_{peak}, and x_j and lower T_∞ result in larger q''_{ind}. The upper bound and lower bound of the heat flux q''_{ind} can then be calculated. Result shows that the variance for the worst case of q''_{ind} due to the extreme case of four measurement errors and uncertainties is less than ±0.04 q''_{ind} at thermocouple 1. This demonstrates the insignificant influence of the measurement errors and uncertainties on the heat flux q''_{ind}.

5 Sensitivity Analysis

The grid spacing, thermocouple location, and thermophysical properties used in the finite difference modeling all contribute to the variation of q''_{ind}. The sensitivity to these factors to the inverse heat transfer solution of q''_{ind} is studied.

5.1 Sensitivity to Grid Spacing. The selection of the number of nodes is a compromise of computational time and accuracy of modeling results. A test matrix with the number of nodes in the heating region $m_1 = 3$, 5, and 9 and the number of nodes in the cooling region $m_2 = 101$, 201, 401, and 801 is selected to analyze the influence of grid spacing on q''_{ind}. Results of q''_{ind} are shown in Fig. 8.

With the finest grid spacing of $m_1 = 9$ and $m_2 = 801$, q''_{ind} is 1.1157 MW/m^2. This is the baseline to study the influence of grid spacing. There is a significant drop of q''_{ind} from 1.1223 to 1.1173 MW/m^2 when m_2 is increased from 101 to 201. The influence of m_1 on q''_{ind} is negligible when $m_2 < 201$. For $m_2 \geq 201$, the discrepancy of q''_{ind} with $m_1 = 3$ and $m_2 = 801$ to the baseline result is very small, less than 0.08%. This indicates that the choice of $m_1 = 3$ and $m_2 = 201$ in Sec. 4.2 is good for both computational efficiency and accuracy.

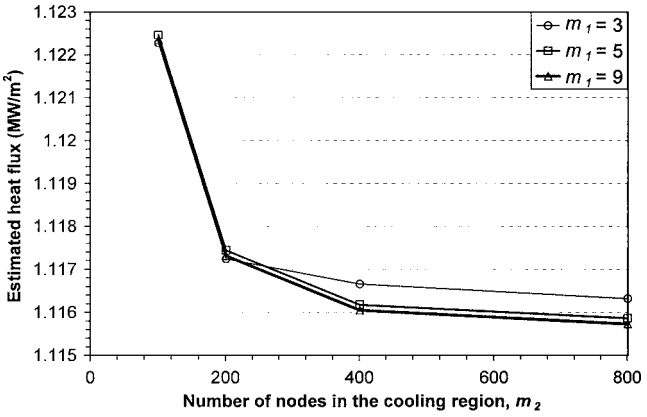

Fig. 8 Effect of grid spacing on the surface heat flux q''_{ind}

5.2 Sensitivity to Thermocouple Location. The sensitivity coefficient of the heat flux is defined as

$$\frac{\partial T(x_j,t_i,q)}{\partial q} \approx \frac{T(x_j,t_i,(1+\eta)q) - T(x_j,t_i,(1-\eta)q)}{2\eta q} \quad (11)$$

where η is a perturbation.

Larger sensitivity coefficient represents that the inverse problem is less sensitive to the measurement errors and more accurate estimates of parameters can be obtained [18]. The sensitivity coefficient of the heat flux for different thermocouples at their own t_{peak} is calculated and compared with each other. When $q''_{ind} = 1.103$ MW/m^2 and $\eta = 10^{-6}$, the thermocouple 1 through 4 exhibits peak temperature at 48.2, 63.7, 159.2, and 401.1 s and has 1.817×10^{-4}, 1.456×10^{-4}, 0.691×10^{-4}, and 0.276×10^{-4} K·m^2/W sensitivity coefficient of the heat flux, respectively. Thermocouple 1 has the largest sensitivity coefficient and is the best location, among four thermocouples, to calculate the heat flux. This is also the thermocouple selected for inverse heat transfer analysis in this study.

5.3 Sensitivity to Thermophysical Properties. In Eqs. (7) and (8), $B = 1.8$ W/m^2·K$^{1.25}$ and $\varepsilon = 0.7$ are used to calculate the heat flux due to the convection and radiation in the finite difference modeling. The influence of uncertainties of these two coefficients on q''_{ind} is investigated by changing the nominal values of B and ε separately. When the B is varied by 0.9 W/m^2·K$^{1.25}$ from its nominal value of 1.8 W/m^2·K$^{1.25}$ and ε is varied by 0.3 from the nominal 0.7, results of the nine estimated q''_{ind} as well as the discrepancy to the nominal value of q''_{ind} (with $B = 1.8$ W/m^2·K$^{1.25}$ and $\varepsilon = 0.7$) are listed in Table 3. The maximal discrepancy is less the 3.6%, which shows that the uncertainties of B and ε have some but not significant effect on q''_{ind}.

6 Finite Element Verification

The accuracy of finite difference model using a single nodal temperature value to represent the temperature distribution of the entire cross section is studied using the finite element method. The actual temperature distribution varies in the radial direction of the workpiece. In the heating region during the heating stage, the temperature difference between the center and surface of the workpiece can be large. Such temperature distribution is quantified using the finite element method. Results from the ANSYS finite element analysis are applied to validate the uniform temperature assumption and accuracy of finite difference modeling.

The AISI 1020 steel rod used in the previous sections for the induction heating experiment and finite difference modeling is meshed using the four-node, four degree-of-freedom quadrilateral axisymmetric elements. The mesh is shown in Fig. 9. Ten elements (eleven nodes) across the radial direction and a total of

Table 3 Influence of the uncertainties of B and ε on the heat flux q''_{ind}(MW/m^2)

	B=0.9 W/m$^2\cdot$K$^{1.25}$		B=1.8 W/m$^2\cdot$K$^{1.25}$		B=2.7 W/m$^2\cdot$K$^{1.25}$	
	q''_{ind}	Discrepancy[a]	q''_{ind}	Discrepancy[a]	q''_{ind}	Discrepancy[a]
ε=0.4	1.100	−1.54%	1.100	−1.54%	1.104	−1.21%
ε=0.7	1.105	−1.11%	1.117	--	1.130	1.12%
ε=1.0	1.131	1.25%	1.144	2.41%	1.157	3.59%

[a]Based on the deviation from the nominal q''_{ind} with B=1.8 W/m$^2\cdot$K$^{1.25}$ and ε=0.7

1260 elements are used in the $0 \leqslant x \leqslant 80.01$ mm area. These elements are 0.635 mm×0.635 mm square shape. In the region of $x > 80.01$ mm, the mesh with 1919 elements is automatically generated by the ANSYS. Mesh in this region has less effect on the simulation results and does not need to be as dense as in the $0 \leqslant x \leqslant 80.01$ mm area.

Along the center axis and in the symmetric plane of the rod (x=0), as shown in Fig. 9, the boundary condition is adiabatic. The heat flux due to radiation and convection, calculated by the same equations as in the finite difference modeling (Sec. 2), is applied on the outer surface. Based on Sec. 4, a constant induction heat flux of 1.200 MW/m^2 is applied on the peripheral surface of the heating region. The induction heating time t_h=25 s.

Results of the finite element analysis at t=15.0, 20.0, and 25.0 s and cross sections at x=0 mm (middle of the heating region), x=5.6 mm (the interface of the heating and cooling regions), and x=30 mm (location of thermocouple 1) are shown in Fig. 10 (marked as FEM). For mutual comparison, the nodal temperature at corresponding positions and time instants are also obtained using the finite difference model (marked as FD model) and plotted as the horizontal dashed lines in Fig. 10.

The finite element method is used to calculate the eleven nodal temperatures in the same cross section. At the cross section x=0 mm when t=15.0 s, the rod center and peripheral temperature is 492.2 and 571.3 °C, respectively. The temperature difference in the cross section is about 80 °C, which is significantly different from the constant cross-section temperature assumption used in the finite difference modeling. The finite difference method estimates that the temperature of the cross section is 538.2 °C. The average of eleven nodal temperatures solved by finite element method is 532.1 °C, which has only 1.1% discrepancy with the finite difference modeling. Similarly, for the cross section at x=0 mm when t=20.0 and 25.0 s, although the difference in temperature between the center and peripheral of the rod is about 80 °C, the nodal temperature obtained from the finite difference method, 635.2 and 720.1 °C, respectively, is also very close to the average temperatures solved using the finite element method at the eleven nodes of the same cross section.

The comparison of results obtained from finite difference method (nodal temperature) and finite element method (average cross-section temperature) at three cross sections (x=0, 5.6, and 30 mm) and three time instants (t=15.0, 20.0, and 25.0 s) is summarized in Table 4. Very good agreement, less than 2.0% discrepancy, can be seen in the cross sections x=0 and 5.6 mm.

In the cross section away from the heating region, the temperature difference between the center and peripheral of the rod becomes smaller. As shown in Fig. 10, at x=5.6 mm, the temperature difference is about 40 °C. At x=30 mm, the temperature distribution is almost uniform with less than 0.2 °C (t=25.0 s) difference from the center to the peripheral surface. This validates the use of a single value to represent the temperature of the cross section in the finite difference formulation to solve the induction heat flux.

7 Conclusions

The explicit finite difference and inverse heat transfer modeling was developed to solve the surface heat flux generated by induction of a long workpiece with low cross section Biot number. Experiments of induction heating of a carbon steel rod were carried out. Measured temperature data provided not only the input for inverse heat transfer solution but also the validation of the

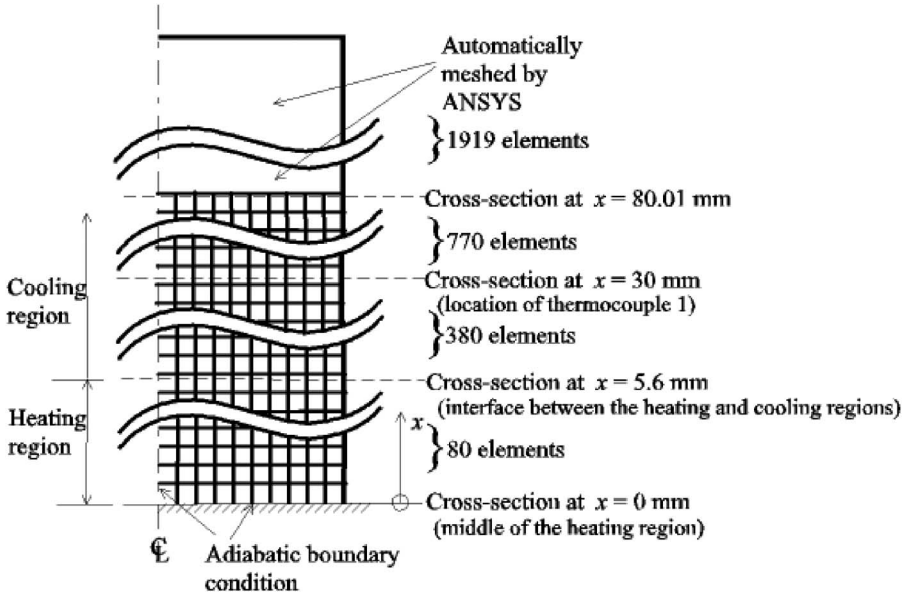

Fig. 9 FEM mesh and the three cross sections

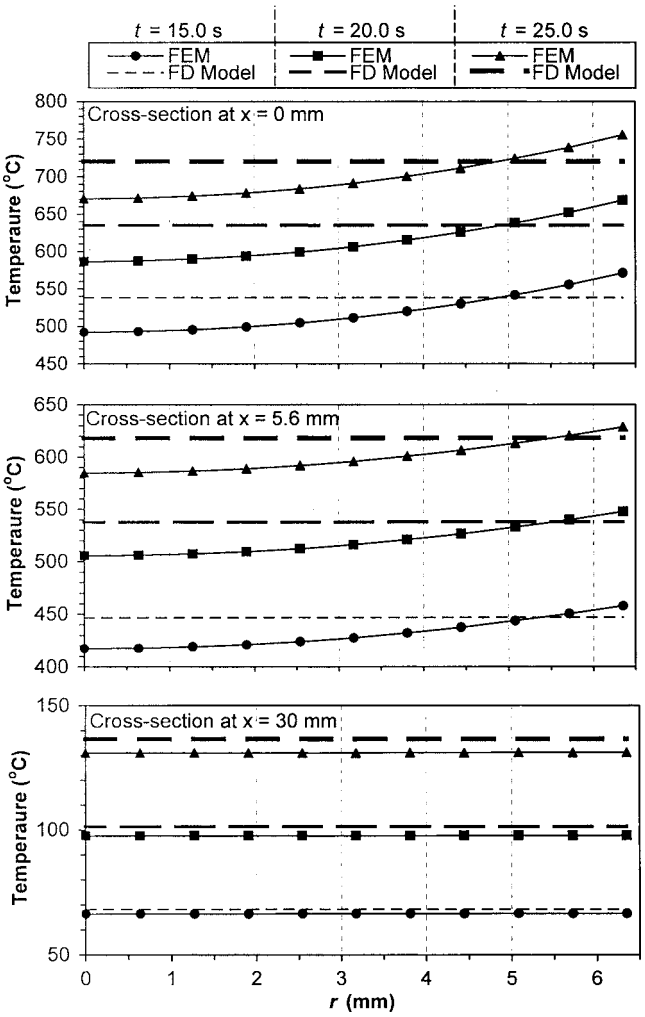

Fig. 10 Comparison of the finite element and finite difference analysis results for t_h=25 s at three cross sections

finite difference model. The sensitivity to the grid spacing, thermocouple location, and thermophysical properties was discussed. The finite element analysis showed significant difference in temperature variation in the cross section during heating and also demonstrated the feasibility to use a single nodal temperature to represent the average cross section temperature in finite difference modeling.

Table 4 Comparison of finite difference nodal temperature and the finite element analyzed average temperature of the cross section

t (S)	Cross section, x (mm)	Finite difference cross-section nodal temperature (°C)	FEM average temperature (°C)	Discrepancy ΔT	Discrepancy (°C) (%)
	0	538.2	532.1	6.1	1.13%
15.0	5.6	446.6	438.0	8.6	1.93%
	30	68.1	66.4	1.7	2.50%
	0	635.2	627.9	7.3	1.15%
20.0	5.6	537.6	527.1	10.5	1.95%
	30	101.2	97.7	3.5	3.46%
	0	720.1	713.7	6.4	0.89%
25.0	5.6	617.9	607.3	10.4	1.68%
	30	136.5	131.0	5.5	4.03%

This study demonstrates the application of inverse heat transfer method to design and analyze the manufacturing process. The finite difference method presented in this study can be enhanced using the implicit formulation, which is expected to improve the computational time.

The method proposed in this study can be applied as a semi experimental method to determine the surface heat flux generated by induction. The temperature data from a thermocouple or infrared sensor can be used as the input for the inverse heating transfer solution of induction heat flux. This heat flux can be the input for induction heating of moving parts with complicated shape. One of the applications of the proposed method is to estimate the induction heat flux and, subsequently, the temperature profile on a rotating tool. The heated tool is used for machining of elastomers, elastomer-steel composites, plastics, and other soft, flexible engineering materials.

Acknowledgment

This research is sponsored by the National Science Foundation and Michelin Americas R&D Corp. Assistance provided by Steve White and discussions with Professor Michael Chen are gratefully acknowledged.

Nomenclature

A_m = area of the cross section at node m
B = coefficient for calculation of convection heat flux q''_{conv}
Bi = Biot number
e_{rms} = root mean square error
c = specific heat
h = convection coefficient
k = thermal conductivity
L = half length of the workpiece
L_c = characteristic dimension of the workpiece
L_h = half width of the heating region
m = node number
m_1 = number of nodes in the heating region
m_2 = number of nodes in the cooling region
N = number of measurements
n_1 = number of time instants
n_2 = number of thermocouples
P_m = perimeter of the cross section at node m
p = time step
q''_{ind} = surface heat flux generated by induction in the heating region
q''_{conv} = surface heat flux due to heat convection
q''_{rad} = surface heat flux due to radiation
r = radius of the rod
T_∞ = ambient temperature
T_{peak} = peak temperature
$T^{t_i}_{x_j|\text{est}}$ = temperatures estimated by finite difference model
$T^{t_i}_{x_j|\text{exp}}$ = experimentally measured temperatures
T^p_m = nodal temperature at node m and time step p
t = time
Δt = time increment
t_i = time instant of an experimental measurement
t_h = duration of heating
t_{peak} = instant for peak temperature
x_j = location of thermocouple j from the center of the rod
Δx = width of the control volume
Δx_h = spacing between two adjacent nodes in the heating region
Δx_c = specing between two adjacent nodes in the cooling region
V_m = volume of the control volume at node m
ε = emissivity
η = perturbation

ρ = density
σ_s = Stefan-Boltzmann constant

References

[1] Brown, G. H., Hoyler, C. N., and Bierwirth, R. A., 1947, *Therory and Application of Radio-Frequency Heating*, Van Nostrand, NY.
[2] Rudnev, V., Loveless, D., Cook, R., and Black, M., 2003, *Handbook of Induction Heating*, Marcel Dekker, NY.
[3] Simpson, P. G., 1960, *Induction Heating*, McGraw-Hill, NY.
[4] Orfueil, M., 1987, *Electric Process Heating*, Battelle Press, Ohio.
[5] Semiatin, S. L., 1986, *Induction Heat Treatment of Steel*, American Society for Metals, Ohio.
[6] Wang, K. F., Chandrasekar, S., and Yang, H. T., 1992, "Finite Element Simulation of Induction Heat Treatment and Quenching of Steel," Trans. North Am. Manuf. Res. Inst. SME, **20**, pp. 83–90.
[7] Wang, K. F., Chandrasekar, S., and Yang, H. T., 1995, "Finite Element Simulation of Moving Induction Heat Treatment," J. Mater. Eng. Perform., **4**(4), pp. 460–473.
[8] Wang, K. F., Chandrasekar, S., and Yang, H. T., 1992, "Finite Element Simulation of Induction Heat Treatment," J. Mater. Eng. Perform., **1**(1), pp. 97–112.
[9] ter Maten, E. J. W., and Melissen, J. B. M., 1992, "Simulation of Inductive Heating," IEEE Trans. Magn., **28**(2), pp. 1287–1290.
[10] Chaboudez, C., Clain, S., Glardon, R., Mari, D., Rappaz, J., and Swierkosz, M., 1997, "Numerical Modeling in Induction Heating for Axisymmetric Geometries," IEEE Trans. Magn., **33**(1), pp. 739–745.
[11] Chaboudez, C., Clain, S., Glardon, R., Rappaz, J., Swierkosz, M., and Touzani, R., 1994, "Numerical Modeling of Induction Heating of Long Workpieces," IEEE Trans. Magn., **30** (6), pp. 5028–5037.
[12] Melander, M., 1985, "Computer Predictions of Progressive Induction Hardening of Cylindrical Components," Mater. Sci. Technol., **1** (10), pp. 877–882.
[13] Kurek, K., Przylucki, R., and Ulrych, B., 1996, "Nonstationary Thermal Field in the Induction Heating System with Axial Symmetry," Acta Tech. CSAV (Ceskoslovensk Akademie Ved), **41**(4), pp. 405–417.
[14] Skoczkowski, T. P., and Kalus, M. F., 1989, "The Mathematical Model of Induction Heating of Ferromagnetic Pipes," IEEE Trans. Magn., **25**(3), pp. 2745–2750.
[15] Labridis, D., and Dokopoulos, P., 1989, "Calculation of Eddy Current Losses in Nonlinear Ferromagnetic Materials," IEEE Trans. Magn., **25**(3), pp. 2665–2669.
[16] El-Kaddah, N., Craen, R., and Loue, W., 1998, "Mathematical Model of Induction Heating of Thixoformable Aluminum Billets," Light Metals, in *Proceedings of the Technical Sessions Presented by the TMS Aluminum Committee at the 127th TMS Annual Meeting, San Antonio, Texas, February 15–19*, pp. 1097–1102.
[17] Kunshchikov, V. G., 1998, "Mathematical Model of Induction Heating of a Cylinder for Computer-Aided Manufacturing (CAM)," J. Eng. Phys. Thermophys., **71**(3), pp. 546–550.
[18] Ozisik, M. N., and Orlande, H. R. B., 2000, *Inverse Heat Transfer*, Taylor & Francis, NY.
[19] Incropera, F. P., and Dewitt, D. P., 2002, *Fundamentals of Heat and Mass Transfer*, Wiley, NY.
[20] Himmelblau, D. M., 1972, *Applied Nonlinear Programming*, McGraw-Hill, NY.
[21] Bringas, J. E., and Wayman, M. L., 2000, *The Metals Black Book*, 4th ed., Casti, Edmonton, Canada.